



# Bimodal mesoporous NiO/CeO<sub>2-δ</sub>-YSZ with enhanced carbon tolerance in catalytic partial oxidation of methane—Potential IT-SOFCs anode

Simona Somacescu<sup>a,\*</sup>, Nicoleta Cioatera<sup>b</sup>, Petre Osiceanu<sup>a</sup>, Jose Maria Calderon-Moreno<sup>a</sup>, Corneliu Ghica<sup>c</sup>, Florentina Neațu<sup>c</sup>, Mihaela Florea<sup>c,d,\*</sup>

<sup>a</sup> “Ilie Murgulescu” Institute of Physical Chemistry, Romanian Academy, Spl. Independentei 202, 060021, Bucharest, Romania

<sup>b</sup> University of Craiova, Department of Chemistry, Calea București 107i, 200478, Craiova, Romania

<sup>c</sup> National Institute of Materials Physics, 405A Atomistilor Street, 077125, Magurele, Romania

<sup>d</sup> University of Bucharest, Faculty of Chemistry, 4 – 12 Regina Elisabeta Bvd., Bucharest, 030016, Romania

## ARTICLE INFO

### Keywords:

Solid oxide fuel cells  
Catalytic partial oxidation of methane  
Carbon tolerance

## ABSTRACT

In the present study we report on the activity, selectivity and stability of the bimodal mesoporous NiO/CeO<sub>2-δ</sub>-YSZ anodes for IT-SOFCs applications. These materials present high concentration of Ce<sup>3+</sup> ions stably retained in the lattice, which proved to be efficient for the catalytic partial oxidation of CH<sub>4</sub> to syngas in the temperature range 600–800 °C. The excellent carbon tolerance was proved by a comprehensive XPS analysis, which monitored the amount of carbon before and after catalytic partial oxidation of methane (CPOM) tests. The mesoporous anodes templated by hexadecyltrimethylammonium bromide (CTAB) and tripropylamine (TPA) were obtained using a hydrothermal synthesis route. The effect of Ni and Ce incorporation on the yttria stabilized zirconia (YSZ) structure, texture, morphology and surface chemistry was discussed and correlated with catalytic and electrochemical behavior. The exhaustive characterization of the bulk and surface properties of the catalysts have been accomplished by means of complementary methods: XRD, SEM / EDX / HRTEM, TGA / TPR, XPS. The electrochemical and catalytic performance were improved when the surface contains more reduced ceria and NiO was formed as secondary phase. These features lead to a large number of vacancies and consequently a better oxygen migration, which facilitate the carbon removal.

## 1. Introduction

One of the main research aims in the field of solid oxide fuel cells (SOFCs) is the attempt to reduce the operating temperature in the range of (600–800 °C). The advantages of a intermediate-temperature operation for SOFCs (IT-SOFC) include wider material choice, better long-term performance, potentially reduced fuel cell costs, a wider range of fuels and increased tolerance to surface impurities. Nowadays, there are many research groups focused mainly on the lowering of the production costs of the units incorporating IT-SOFC stacks and considerable progress has been made over the last 10 years for the development of fuel cells to operate with good performance in intermediate temperature (600–800 °C).

Therefore, the development of optimal materials and synthesis routes for anodes are highly desired leading to lower cost processes that yields stable and reliably high electrical performance. In this regard a great variety of anodic materials have been developed. Anode materials

work in reducing environments and are flexible for a wide range of fuels such as H<sub>2</sub>, CH<sub>4</sub>, CO natural gas and other hydrocarbons and must be tolerant to carbon deposits, S-impurities and reoxidation [1,2].

Using methane as a fuel in SOFC is an alternative to H<sub>2</sub>-based technology [3–5] and a special interest is still dedicated to the exploitation of highly abundant natural gas reserves by a green route. Nevertheless, H<sub>2</sub> remains the most efficient and environmentally friendly fuel but generating and its storage are still considered major drawbacks. Widening the applicability of SOFCs that work with CH<sub>4</sub> or other fuels such as biogas or bioalcohols is suitable due to their high efficiency and the fact that the gases mainly contain CO<sub>2</sub> and H<sub>2</sub>O and CO + H<sub>2</sub>, respectively. CO<sub>2</sub> can easily be separated and liquefied which leads to minimized carbon emissions while the CO + H<sub>2</sub> mixture is involved in the Fischer-Tropsch process to obtain aliphatic products.

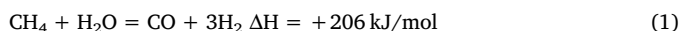
Methane can be converted via two pathways: i) direct conversion by oxidation to added value compounds (i.e. methanol, formaldehyde) or by oxidative coupling to ethylene and ii) indirect conversion to other

\* Corresponding author at: National Institute of Materials Physics, 405A Atomistilor Street, 077125, Magurele, Romania.

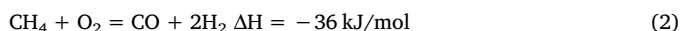
\*\* Corresponding author.

E-mail addresses: [ssimona@icf.ro](mailto:ssimona@icf.ro) (S. Somacescu), [mihaela.florea@chimie.unibuc.ro](mailto:mihaela.florea@chimie.unibuc.ro), [mihaela.florea@infim.ro](mailto:mihaela.florea@infim.ro) (M. Florea).

products via synthesis gas, by steam reforming, dry reforming and catalytic partial oxidation of methane (CPOM). The steam reforming is the mainly practical route for the methane conversion at the present time (Eq. (1)) [6,7]



The main drawbacks of this process are the endothermicity and the residence time inside the reactors, large reactor volumes being necessary for the industrial scale. Therefore, the exothermic catalytic methane partial oxidation (CPOM) represents an alternative for the syngas production. In this process, methane is converted with oxygen to form  $\text{H}_2$  and CO (Eq. (2)) in one step reaction:



Different transition metals (Ni, Co and Fe) [8–10] and noble metals (Ru, Rh, Pd, Pt, Ir) [11–15] have been reported as active catalysts for the partial oxidation of methane. Nevertheless, nickel is doubtless the most widely used active phase for partial oxidation of methane, one reason being its low cost. However, the materials used as anode in IT-SOFCs should catalyze efficiently the fuel oxidation, possess stability in reducing environment, be an electrical conductor and have a sufficient degree of positioning to ensure access of gaseous species to the electrolyte/anode interface. A considerable interest is related to safely working within the range of temperature used for fuel and air, as well. Milewski et al. [16] optimized SOFC hybrid system and they found that the temperature should be kept constant on 800 °C and gas turbine inlet at the maximum temperature of 1100 °C.

The development of new catalytic mesoporous materials that allow the control of the nanocrystalline framework can represent an effective pathway to incorporate high concentrations of metal throughout porous materials during soft chemistry synthesis [17]. The synthesis procedure of anode can affect its activity and selectivity to a great extent. A large number of studies concerning the synthesis of anode materials with different structures in order to improve the anode performance have been reported. Thus, as anodes were developed alternative materials with different structure: fluorite [18–20] perovskite [21,22], titanates [23–25], spinel structure [26] pyroclor [27,28] and composite materials. Prasad et al. [29] obtained 40 vol.% NiO–CGO composite by glycine-nitrate-process (GNP) at 1400 °C for 2 h and assessed the catalytic performance for steam reforming of methane (SRM). They found that the nickel nano-particles mainly located on the surface of CGO assure a strong interaction with the support and thus the carbon formation is suppressed. Da Silvas et al. [30] synthesized Ni-based catalysts supported on Gd, Y, Pr, Zr, Nb doped  $\text{CeO}_2$  by hydrothermal method and studied the effect of dopant on the anode performance for ethanol internal reforming. They demonstrated that the  $\text{NiNb}_2\text{O}_6$  phase covers the Ni particles and thus the carbon formation is inhibited. Vert et al. [31] studied the anode performance of Ni and Sr incorporation in  $\text{LaCrO}_3$  in symmetrical cells. The synthesized anodes by Pechini method were calcined at 1050 °C for 10 h using several calcinations steps to minimize the presence of impurities. Thus, a 30% methane conversion at 900 °C for SRM on  $\text{La}_{0.85}\text{Sr}_{0.15}\text{Cr}_{0.9}\text{Ni}_{0.1}\text{O}_{3-\delta}$  reduced at 800 °C was obtained.

In light of these findings, the incorporation of nickel, due to its catalytic role [29,30,32–34], and ceria which possesses  $\text{Ce}^{3+}$  [35,36] to increase of the ionic conduction, into YSZ lattice by direct synthesis route could improve the materials' properties as anode for IT-SOFC.

In this paper, we report on the activity, selectivity and stability of the bimodal mesoporous  $\text{NiO/CeO}_{2-\delta}$ -YSZ (5, 10, 15 mol.% NiO, 20 mol.%  $\text{CeO}_2$  and 10 mol.%  $\text{Y}_2\text{O}_3$ ) anodes for the catalytic partial oxidation of  $\text{CH}_4$  to syngas in the temperature range 550–800 °C at atmospheric pressure. The effect of the Ni and Ce incorporation on the structure, texture, morphology and surface chemistry of yttria stabilized zirconia (YSZ) was discussed and correlated with catalytic and electrochemical behavior. The low amount of carbon deposition, before

and after catalytic tests, was monitored by XPS analysis method. We proved that the bimodal mesoporous materials exhibit a good Ni and Ce dispersion into YSZ lattice, favored by a facile synthesis protocol with low effective cost, as well as an excellent carbon tolerance. It is well known that the delamination of the anode can also occur due to thermal mismatch between cermet anode and ceramic electrolyte induced by a higher amount of Ni. On the other hand, MIEC ceramic anode materials (with higher thermal and chemical compatibility with electrolyte) exhibit low electrical conductivity. In order to increase the conductivity and catalytic activity of MIEC materials, the development of the new composites with lower nickel content and well organized mesostructure for a proper transport of the reactant gases through the catalyst layer was our main goal in this study

## 2. Experimental

### 2.1. Synthesis

$\text{NiO/CeO}_{2-\delta}$ -YSZ (5, 10, 15 mol.% NiO, 20 mol.%  $\text{CeO}_2$  and 10 mol.%  $\text{Y}_2\text{O}_3$ ) materials were obtained by a hydrothermal route, using hexadecyltrimethylammonium bromide (CTAB) and tripropylamine (TPA) as templates. The synthesis started by a very good dispersion of the hexadecyltrimethylammonium bromide (CTAB) in deionized water leading to the formation of micellar solutions. Zirconium oxychloride ( $\text{ZrOCl}_2$ , Riedel deHaën), yttrium nitrate hexahydrate ( $\text{Y}(\text{NO}_3)_3 \cdot 6\text{H}_2\text{O}$ , Merck), cerium (III) nitrate hexahydrate (Merck) and nickel (II) nitrate hexahydrate (Sigma Aldrich) were used as inorganic precursors. The water solutions of the inorganic precursors and urea 99.8% (Alpha Aesar) were added to micellar solutions. The molar ratio of surfactant/urea was 1:2. After 2 h under strong stirring 6 ml tripropylamine (Sigma Aldrich) was added. After 3 h the pH value was adjusted to 12 using tetrabutylammonium hydroxide solution ~40% in water (Sigma-Aldrich) (TBAOH) at room temperature and left for aging 12 h. The solutions have been loaded into teflon link steel autoclave equipped with pressure gauge and heated at 120 °C for 24 h, maintaining the stirring. All the precipitates with greasy aspect were filtered, alternately washed with water and ultrasonicated in ethanol, dried at 100 °C for 12 h and calcined in air at 800 °C. The samples were labelled function of Ni content N1 (for 5% Ni), N2 (for 10% Ni) and N3 (for 15% Ni). In order to illustrate an effect of higher Ni content on catalytic performance, our preliminary results obtained for a sample containing 30 mol.% Ni (N4) conducted us to the conclusion that the synthesis protocol should be optimized for higher Ni amount (see Supplementary Materials). Briefly, although N4 sample shows an ordered mesoporous structure but with a diminished specific surface, the catalytic activity was lower than N3 but a very good carbon tolerance was highlighted. The evaluation of the catalytic and electrocatalytic performance for higher Ni content, up to 30 mol. % will be the subject of the subsequent study.

### 2.2. Characterization

**X-Ray diffraction analysis** was carried out on a Bruker-AXS D8 Advance diffractometer equipped with a one-dimensional detector (LynxEye type) using  $\text{Cu-K}\alpha$  radiation (0.1541 nm) at a scanning speed of  $0.10^\circ \text{ min}^{-1}$  in the 20–80° 2 $\theta$  range. Phase identification was performed using ICSD database.

**The differential thermal and thermogravimetric analysis** of the as-synthesized powders was accomplished by using a TG-DTA analyzer Shimadzu DTA-60 instrument. The experiments were performed in nitrogen atmosphere from room temperature to 900 °C with a heating rate of  $10^\circ \text{C min}^{-1}$ , by using alumina as reference.

**$\text{N}_2$  adsorption/desorption** – The characterization of the porous texture of the as-synthesized and calcined samples was performed by  $\text{N}_2$  adsorption at  $-196^\circ \text{C}$  using a Micromeritics instrument (ASAP 2010). The Brunauer-Emmett-Teller (BET) method was used to calculate the

surface area from the data obtained at  $P/P_0$  between 0.01 and 0.995. Prior to surface area determination, the samples were outgassed at 150 °C for 5 h. The pore size distribution of each sample was determined from the desorption branch of the  $N_2$  isotherm.

**Scanning electron microscopy (SEM)** was carried out on a Field Emission Gun FEI Quanta 3D microscope operating at 2 kV equipped with energy dispersive X-ray spectrometer (EDX). The EDX spectra were collected using an accelerating voltage of 30 kV.

**Transmission electron microscopy (TEM).** The sample has been analyzed using a JEM ARM 200F probe corrected TEM operated at 200 kV. The instrument can be operated in TEM / STEM modes and is provided with a JED 2300 Si/Li EDS detector with a spectral resolution of 133 eV. TEM/HRTEM and SAED modes have been used for morphological and structural characterization, while the measurements for the local chemical composition have been performed by STEM-EDS mapping.

The **temperature programmed reduction measurements** in hydrogen atmosphere (TPR- $H_2$ ) were conducted on a Micromeritics, AutoChemII 2920 apparatus. Approximately 20 mg samples were pre-treated at 150 °C (in an air flow of 30 ml min<sup>-1</sup> for 1 h) and then cooled to room temperature in argon gas flow before reduction. A hydrogen–argon mixture (10%  $H_2$ ), was used to reduce the samples at a flow rate of 50 ml/min. The temperature was linearly raised at a rate of 10 °C min<sup>-1</sup> up to 950 °C.

**X-ray photoelectron spectroscopy (XPS)** – Surface analysis performed by X-ray photoelectron spectroscopy (XPS) was carried out on PHI Quantera equipment with a base pressure in the analysis chamber of 10<sup>-9</sup> Torr. The X-ray source was monochromatized Al K $\alpha$  radiation (1486.6 eV) and the overall energy resolution is estimated at 0.6 eV by the full width at half-maximum (FWHM) of the Au4f<sub>7/2</sub> photoelectron line (84 eV). The unavoidable charging effect was minimized by using a dual beam (electrons and Ar<sup>+</sup> ions) as neutralizer and the spectra were calibrated using the C1s line (BE = 284.8 eV) of the adsorbed hydrocarbon on the sample surface (C–C or (CH)<sub>n</sub> bondings).

### 2.3. Electrochemical characterization

Ionic conductivity was measured using two-point probe impedance spectroscopy technique under reducing atmosphere (a mixture of 4%  $H_2$ /Ar). In this respect, powders were shaped into pellets by uniaxial pressing, followed by thermal treatment at 800 °C for 12 h. The as-obtained pellets were characterized by XRD and SEM-EDXS analysis. The impedance measurements were performed with a Zhaner IM6eX analyzer in the 3 MHz–0.10 Hz frequency range. Gold was used as electrode. The amplitude of the AC perturbation signal was 50 mV. The set-up was equilibrated under reducing atmosphere at 800 °C overnight. Measurements were carried out in the temperature range 300–800 °C.

### 2.4. Catalytic activity measurements

The catalytic partial oxidation of methane (CPOM) was evaluated in a continuous fixed-bed tubular reactor (length of 300 mm and i.d. of 9 mm, Hastelloy X tube), equipped with a thermo well in the center of the catalyst bed. The experiments were typically carried out in a downflow system at atmospheric pressure. The catalyst powder was placed between a two layers of quartz wool and was first activated for 2 h in air, at 800 °C before the reaction, and then the reactor was cooled down to 200 °C. Reactions were conducted at different temperatures starting from 200 °C, using a feed consisting of 13.33%  $CH_4$ ; 6.66%  $O_2$ ; 80%  $N_2$  at a total flow of 37.5 ml min<sup>-1</sup> and GHSV of 22,500 h<sup>-1</sup>. The products were analyzed online by a gas chromatograph (Shimadzu GC-2014) equipped with a TCD and FID detectors and two capillary columns Molecular Sieve 5A and Poraplot Q (length, 60 m; internal diameter, 0.32 mm; film thickness, 0.5  $\mu$ m). Activity and selectivity results were calculated according to the equations given below:

$$CH_4 \text{ conversion (\%)} = \frac{\mu_{CH_4in} - \mu_{CH_4out}}{\mu_{CH_4in}} \times 100$$

$$CO \text{ selectivity (\%)} = \frac{\mu_{CO}}{\mu_{CH_4in} - \mu_{CH_4out}} \times 100$$

## 3. Results and discussion

Thermal analysis of N1, N2, N3 “as prepared” powders was performed under nitrogen atmosphere in the 30–900 °C range and the obtained results are presented in Fig. SI 1. The studied samples show an initial weight loss (TG curves) of around 10 wt% upon heating up to 150 °C due to the elimination of species such as adsorbed water and surface OH groups. By increasing the temperature an additional weight loss of 25% is recorded for all samples until 400 °C. This weight loss is accompanied by an exothermic DTA profile between 150 and 400 °C being correlated with the decomposition of organic residues used during the synthesis and the crystallization of cerium oxide. As previously shown [37] the elimination of the organic part takes place through an oxidation reaction, an exothermic process, maintained by the oxygen from ceria lattice.

After 400 °C no notable modifications were observed in TG and DTA profiles. Taking into account that the catalytic reactions were performed at max. 800 °C, our previous results [35] and the ones from thermal analysis, we decided that the optimum calcination temperature for all samples to be 800 °C.

### 3.1. XRD-EDX

The XRD patterns of N1, N2 and N3 “as prepared” powders (Fig. 1) correspond to a main phase with fluorite-type symmetry, space group *Fm-3m*. The (200) and (400) diffraction planes of the main phase, stabilized zirconia, at  $\sim 34$  and  $73^\circ$ , respectively (see Fig. 1b and c), show a single maximum for all samples, which corresponds to a cubic lattice.

XRD also detects the presence of bunsenite – NiO, space group *Fm-3m* with the main features at  $\sim 43^\circ$ ,  $37^\circ$  marked with “x”. These features are barely distinguishable in N1 (Fig. 1), therefore Ni present in N1 is incorporated in the cubic fluorite-type phase, although XRD evidence cannot exclude the presence of very small NiO crystallites out of the fluorite structure. The increase of Ni content leads to the growth of NiO peaks, which are clearly visible in N2 and N3 (Fig. 1). There is a clear shift of the main phase peaks to lower angles from N1 to N3. The lattice parameter for the equivalent cubic lattice,  $a$ , indicative of the cell volume, defined as  $a = \sqrt{3}d_{111}$ , where  $d_{111} = \lambda/2\sin\theta_{111}$ ,  $\lambda$  is the wavelength of the CuK $\alpha$  radiation ( $\lambda = 1.5405 \text{ \AA}$ ) and  $\theta_{111}$  the position of the 111 peak ( $2\theta_{111} \sim 30 \text{ deg}$ , Fig. 3a), for the three samples, increases from  $a = 5.192(7) \text{ \AA}$  in N1 to  $a = 5.224(1) \text{ \AA}$ , in N3 [38].

The crystallite sizes for the main fluorite-type phase, calculated by

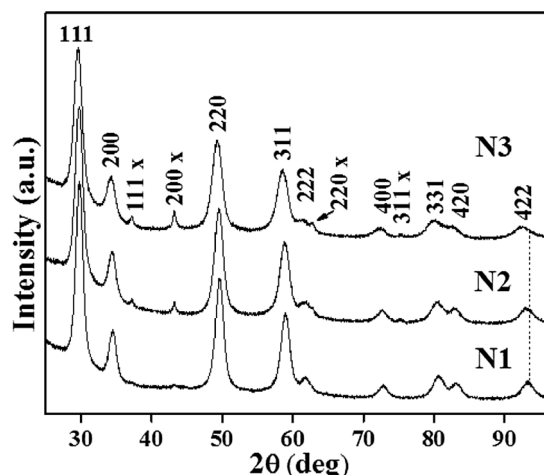


Fig. 1. XRD patterns of samples N1 (a), N2 (b), N3 (c).

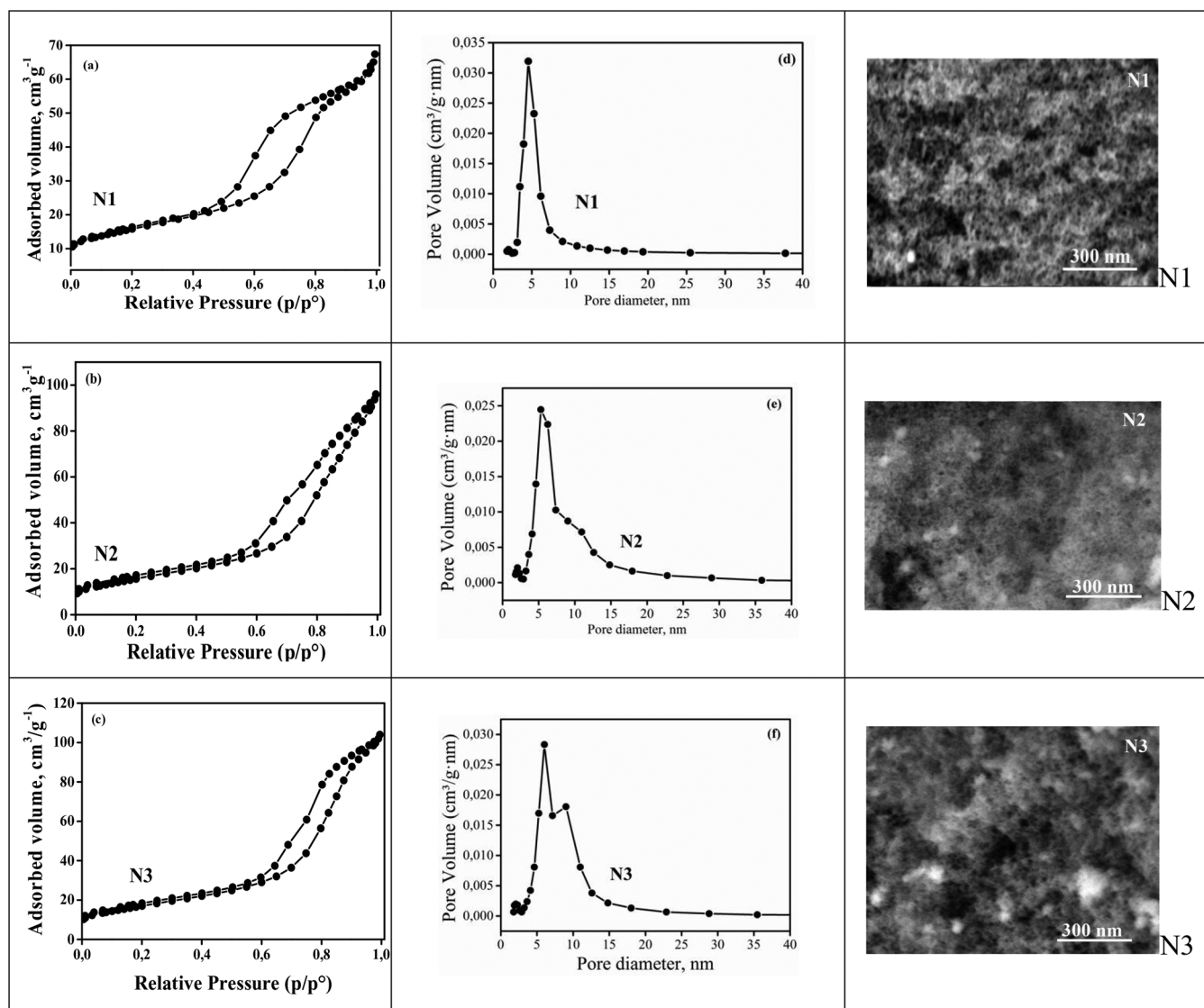


Fig. 2. Adsorption-desorption isotherms (a–c), pore size distribution (d–f) and SEM micrographs for N1, N2, N3 “as prepared” powders.

Scherrer's method from the peak width of the main XRD feature (111) at  $\sim 30^\circ$ , decrease with Ni content, with values of 7.4, 6.6, and 6.0 nm for N1, N2 and N3, respectively. On the other hand, the crystallite sizes for NiO calculated in N2 and N3 from their main peak (200) at  $\sim 43^\circ$  are  $\sim 12$  nm. The smaller size of the fluorite structure nanocrystallites compared to single oxide NiO can be explained by the inhibition of crystal growth rate in the multioxide phase, accommodating four different cations: Zr, Y, Ce and Ni. Additionally, it is worth to observe, based on the TEM-STEM-EDS analysis, a tendency of NiO segregation from the subsurface/bulk region to the outermost surface layer with a tendency to agglomerate and form nanocrystallite clusters on the surface.

The elemental composition was determined from EDX analysis, as follows: the content of Ni approaches the theoretical values for N1 (5.3 at%), N2 (10.5 at%) and N3 (13.3 at%).

### 3.2. Textural analysis and morphology

BET isotherms of adsorption-desorption of the “as prepared” powders calcined at  $800^\circ\text{C}$  and the Barrett Joyner Halenda (BJH) pore size distributions are shown in Fig. 2(a–f). For all samples it was found the type-IV isotherm hysteresis loop which confirms that the mesoporosity was obtained. The capillary condensation step at relative pressures of

(0.4–0.6) suggests a uniform pore size distribution for the sample with the lowest nickel content (N1) (Fig. 2a). It was observed a decrease of the loop hysteresis by increasing the Ni amount (Fig. 2b, c) and the hysteresis appears at higher relative pressures. Moreover, two distinct capillary condensation steps at a relative pressure ( $P/P_0$ ) range of 0.5–0.7 and 0.7–0.9 respectively, indicate the presence of two different size mesopores, which is also evidenced in the BJH pore size distribution profiles (Fig. 2e, f). In addition, through BJH calculation formalism, the pore size distribution became broader. Thus, two peaks for pore size distribution from the desorption branch centered at  $\sim 6$  and  $\sim 11$  nm, respectively are displayed for the samples with increased Ni content (N2, N3 samples) (Fig. 2e, f). The presence of the bimodal-pores can be ascribed to the structural rearrangement which favors the formation of NiO as secondary phase, as it was confirmed by XRD. On the other hand, these structural and textural rearrangements greatly improve surface area, as calculated by using the Brunauer-Emmett-Teller (BET) method, for the N2 and N3 samples. The surface area of each sample is shown in the Table 1 and increases in the sequence of N1 ( $46.5\text{ m}^2\text{ g}^{-1}$ ) < N2 ( $56.8\text{ m}^2\text{ g}^{-1}$ ) < N3 ( $61.4\text{ m}^2\text{ g}^{-1}$ ), in agreement with the crystallite size calculated using Scherrer equation, which decreases in the same series  $\text{N1} > \text{N2} > \text{N3}$ . Thus, it is expected that the bimodal mesopores distribution leads to a proper transport of the reactant gases through the catalytic layer.



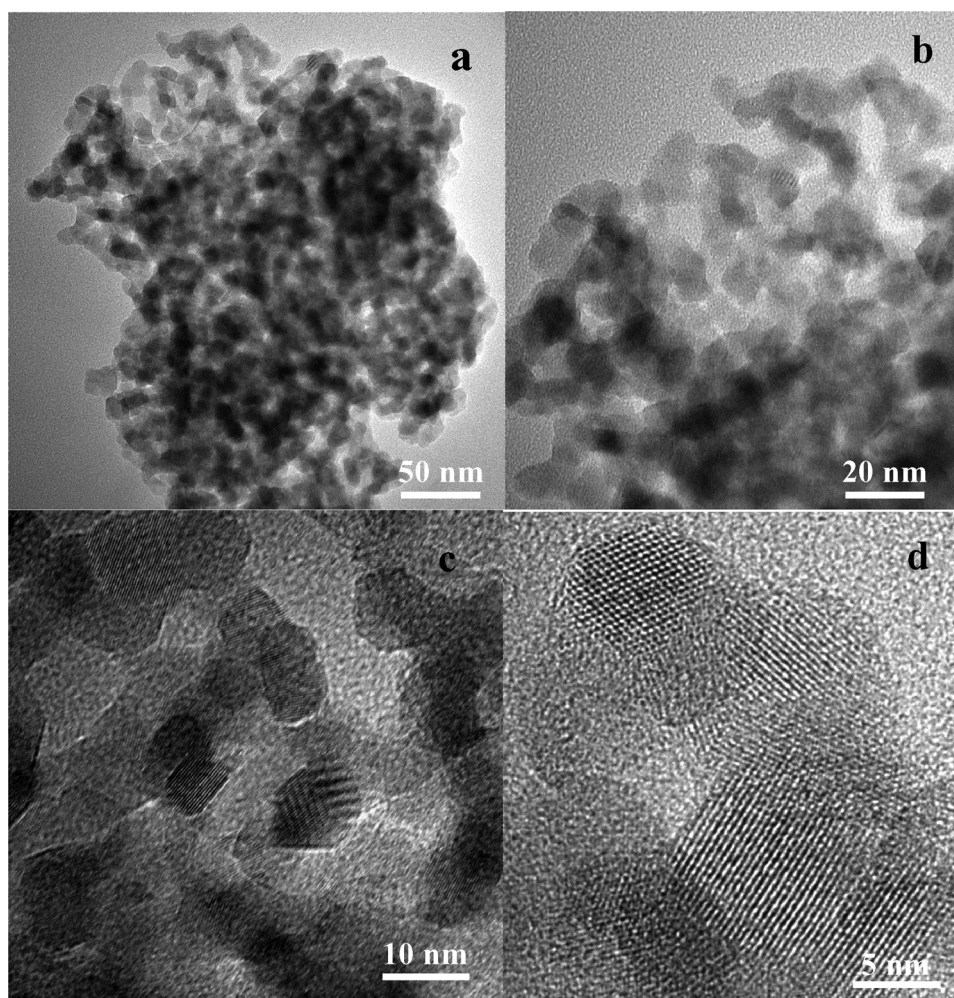


Fig. 3. (a, b) TEM and (c, d) HRTEM micrographs from the sample N1.

**Table 1**

BET surface area, pore size and adsorbed volume of the N1, N2, N3 “as prepared” powders.

Sample	BET surface area ( $\text{m}^2 \text{g}^{-1}$ )	Pore volume* ( $\text{cm}^3 \text{g}^{-1} \text{nm}^{-1}$ )	Adsorbed volume ( $\text{cm}^3 \text{g}^{-1}$ )	Average pore size diameter (nm)
N1	46.5	0.102	69	6
N2	56.8	0.150	98	6/11
N3	61.4	0.163	110	6/11

**SEM** Micrographs of the “as prepared” samples N1, N2, N3 (Fig. 2) show very fine nanopowders, with a porous structure typical of crystalline framework mesoporous materials. SEM measurements determined the homogeneity of the nanopowders microstructure, morphology and texture in all three samples, without formation of agglomerates. The nanoparticle sizes and interparticle pores are in the range of a few nm, in good agreement with nanocrystallite sizes determined from XRD. Nevertheless, additional, more refined HRTEM analysis is compulsory in order to clearly determine the texture, nanocrystalline morphology and chemical composition of the mesoporous powders at the nanoscale, relevant for the catalytic properties.

**TEM** Fig. 3 shows micrographs at different magnifications of the “as prepared” powder N1. The powder consists of single nanocrystallites forming mesoporous aggregates (Fig. 3a and b), leaving pores between individual nanocrystallites similar or smaller than nanocrystallite sizes. The HRTEM micrographs reveal a high crystallinity of the powders,

with very well defined lattice images of the stabilized cubic YSZ nanocrystallites (Fig. 3c and d).

The TEM images in Fig. 4a and c reveal that sample N3 consists in agglomerated nanograins of ca. 8–10 nm generating a nanoporous microstructure. The crystal structure information from the associated SAED pattern indicates the formation of cubic YSZ as predominant phase, generating the set of diffraction rings. The diffuse aspect of the diffraction rings is in agreement with the nanometric size of the YSZ nanoparticles. The HRTEM image in Fig. 4d confirms the formation of cubic YSZ phase. A 10 nm YSZ nanograin in  $[110]_{\text{YSZ}}$  orientation may be noticed, showing well defined facets parallel to the  $(111)_{\text{YSZ}}$  and  $(110)_{\text{YSZ}}$  crystallographic planes. Besides the diffraction rings, scattered diffuse diffraction spots may also be observed. They have been identified as belonging to cubic NiO which is present as minor secondary phase. The Miller indices corresponding to the  $(111)_{\text{NiO}}$  and  $(200)_{\text{NiO}}$  planes of the cubic NiO structure are shown next to the white arrows pointing scattered diffraction spots next to the YSZ diffraction rings.

The chemical composition and homogeneity of the sample have been investigated by EDS mapping in STEM mode. In Fig. 5 we present the STEM-EDS results on the same agglomerate analyzed in Fig. 4.

The STEM ADF image confirms the nanoporous microstructure of the sample, with grains and pores of the same order of magnitude (below 10 nm). The elemental mapping of Zr, O, Y and Ce obtained by selecting well separated EDS peaks indicates a homogeneous distribution of the 4 elements corresponding to the formation of Ce-doped YSZ as predominant phase. However, the fifth detected element, Ni, shows a clear spatial segregation. This goes in line with the observation of



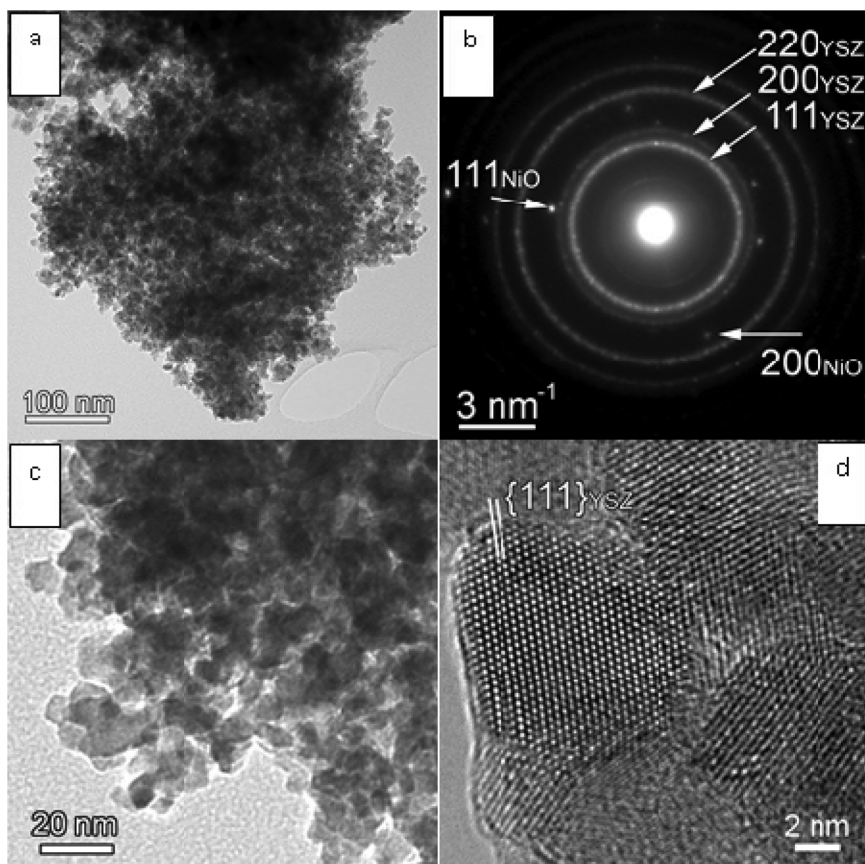


**Fig. 4.** (a) Low-magnification TEM image showing nanostructured agglomerate from the sample N3. (b) Associated SAED pattern proving the formation of cubic YSZ as prevailing structural phase and traces of cubic NiO as secondary phase. (c) TEM image showing the morphology of the N3 powder nanograins. (d) HRTEM image of cubic N3 powder nanograins.

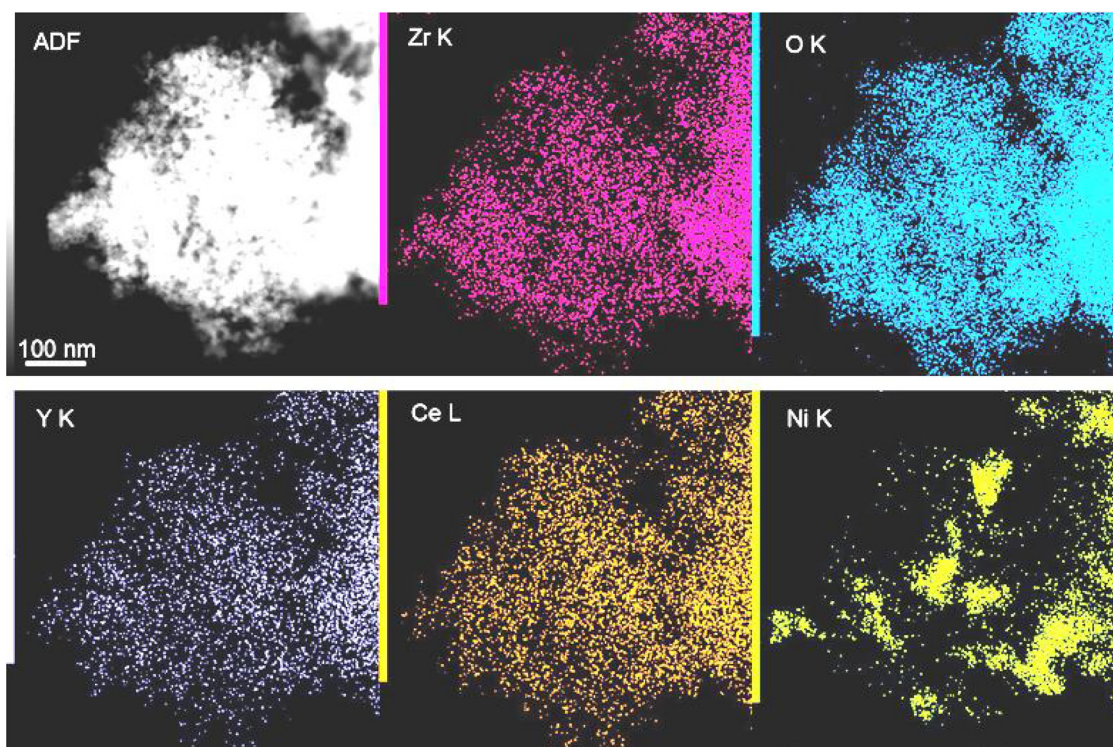


**Fig. 5.** STEM ADF image of a nano-structured agglomerate from sample N3 and the corresponding EDS elemental mapping of Zr, O, Y, Ce and Ni. The following distinct peaks have been chosen for mapping and quantitative analysis: Zr K at 15.7 kV, O K at 0.5 kV, Y K at 14.9 kV, Ce L at 4.8 kV and Ni K at 7.5 kV.

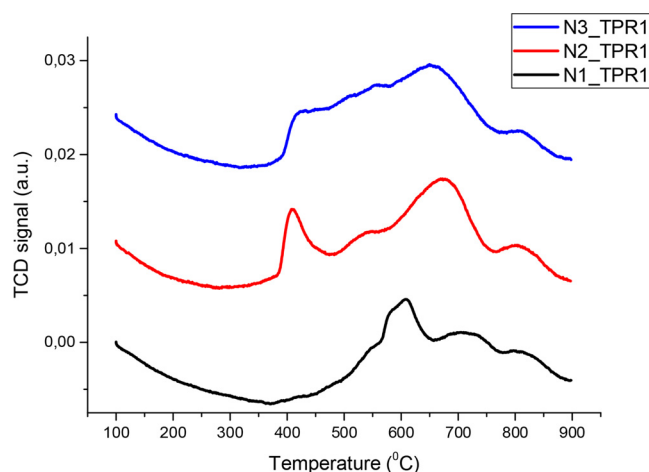


Fig. 6. H<sub>2</sub> TPR profiles after the first cycle for N1, N2 and N3 powders.

scattered diffraction spots assigned to cubic NiO secondary phase in the SAED pattern and of diffraction line at 43° specific for NiO in XRD pattern. Nevertheless, from the two results (SAED and EDS mapping) one still cannot estimate what fraction of the Ni quantity is present as NiO and how much of Ni stands as doping element. The standard less quantitative analysis of the EDS spectrum extracted from the data cube corresponding to the whole image area indicates the following elemental composition: Zr 43.9 at%, Y 23.7 at%, Ce 20.1 at% and Ni 12.3 at%, which is in very good agreement with the overall composition measured by SEM-EDX on the as-prepared N3 powder. Our analytical TEM/STEM preliminary results for a sample containing 30 mol.% Ni are shown in the Supplementary material (S11–S15)

### 3.3. H<sub>2</sub>-TPR

Temperature programmed reduction experiments in H<sub>2</sub> (TPR-H<sub>2</sub>) were carried out in two cycles in order to characterize both surface and bulk oxygen lattice reducibility of the “as prepared” samples. The reduction profiles after the first TPR cycle are shown in Fig. 6.

The profiles consist into two regions corresponding to the reduction of the different types of Ni species as well as Ce species. The low temperature region from 300 to 500 °C corresponds to the reduction of Ni<sup>2+</sup> and Ce<sup>4+</sup> surface species [39,40] while the high temperature region from 500 to 850 °C appears due to the reduction of nickel species from the stabilized YSZ lattice and reduction of Ce<sup>4+</sup> bulk species [41,42]. This is also in good agreement with the TPR profiles of the standard materials presented in the supporting information (Fig. SI 2). It is interesting to note that the N1 sample TPR profile presents reduction peaks only in the high temperature region, in good agreement with the X-ray diffraction data, which reveals for this sample only a main phase with fluorite-type symmetry, attributed to stabilized cubic YSZ. The reduction temperature at about 610 °C, which is not present in the standard materials, can be attributed to the reduction of nickel existing in a strong interaction within the solid solution.

By increasing the Ni loading, a reduction peak appears in the low temperature region, at 412 °C, attributed to the reduction of Ni<sup>2+</sup> species from NiO segregated on the surface. This result is also supported by XRD and XPS analysis, which present specific lines corresponding to NiO and Ni<sup>2+</sup> species, respectively. Nevertheless, the contribution of the reduction of Ce<sup>4+</sup> surface species cannot be ruled out, taking into account the reduction temperature for surface species observed in the standard material (380 °C). The high temperature region of the samples with higher Ni content presents a peak which is shifted to higher temperatures of about 50 °C indicating an even stronger interaction of the Ni with the solid solution (675 °C). All samples present the highest reduction temperature peak at about 800 °C

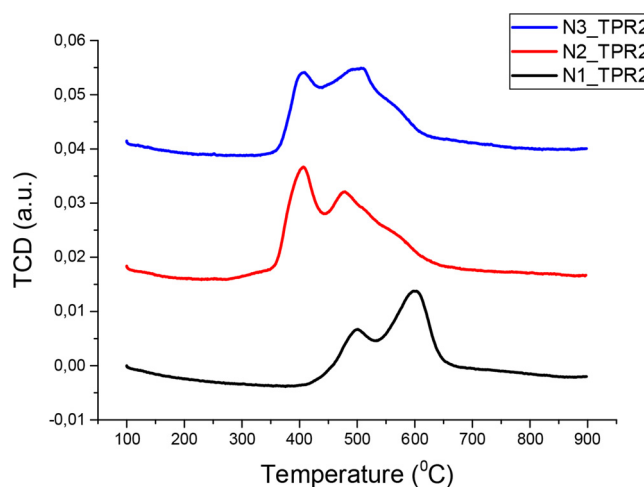


Fig. 7. The second cycle H<sub>2</sub> TPR profiles for N1, N2 and N3.

which may be assigned to the reduction of Ce<sup>4+</sup> bulk species. Nevertheless, this temperature is lower than the one presented in the CeO<sub>2</sub> standard material, indicating a higher oxygen mobility for the Ni containing samples. It seems that the NiO particles can facilitate the reduction of CeO<sub>2</sub> through a H<sub>2</sub> spillover effect during TPR [43,44] or which acts as catalyst in the CeO<sub>2</sub> reduction leading to a shift of the H<sub>2</sub> consumption peaks to lower temperatures [45].

Summarizing, the TPR results confirmed the formation of NiO crystallite for higher Ni loadings and also the fact that Ni was incorporated totally for N1 and partially for N2 and N3 samples in the cubic YSZ structure. The second TPR cycle measurement for all samples was performed after the treatment in O<sub>2</sub>/He at 500 °C and the profiles are shown in Fig. 7. The oxidation treatment was chosen to mimic the reaction conditions (oxidation-reduction) and to reveal the properties of these materials in such conditions. The choice of this temperature was based on the results obtained by Graziani et al. who studied the O<sub>2</sub> uptake on a reduced CeO<sub>2</sub>–ZrO<sub>2</sub> solid solution by the pulse method, and showed that 500 °C was required to re-oxidize the solid solution [42].

The TPR profile of the second cycle for N1 sample presents two reduction peaks at lower temperatures as compared with the first reduction cycle, indicated a higher oxygen mobility. This feature can be related to the Ni re-location or to the interaction nature with the lattice, after the first reduction cycle. Therefore, whereas the Ni seems to be very strong bonded in the lattice, as evidenced by the first TPR-H<sub>2</sub> cycle, after the re-oxidation, the NiO crystallites may be migrated to the surface in the second cycle or is less bonded in the lattice [40]. A similar behavior is observed for N2 and N3 sample, for the peak located at higher temperatures which is shifted from 675 °C in the first cycle to 481 °C in the second cycle for N2 and to 510 °C for N3 sample, respectively.

To sum it up, for all samples in the second TPR cycle, the peak corresponding both to the Ni<sup>2+</sup> from the stabilized YSZ and bulk Ce<sup>4+</sup> species is shifted to lower temperature, probably due to the same re-distribution over new sites of lower energy brought out to the surface during oxidation [46].

The quantitative assessment of the H<sub>2</sub> consumption after the first TPR cycle is presented in Table SI 1. As expected the total H<sub>2</sub> uptake is increasing with the increasing of the Ni content, while the amount of H<sub>2</sub> consumed for the reduction of Ni species from the YSZ lattice is almost the same.

### 3.4. XPS analysis: surface chemistry and quantitative assessment

The most prominent transitions of the elements detected on the outermost surface layer (< 10 nm) were collected as high resolution photoelectron spectra: C1s, O1s, Ce3d, Y3d, Zr3d and Ni2p3/2. The



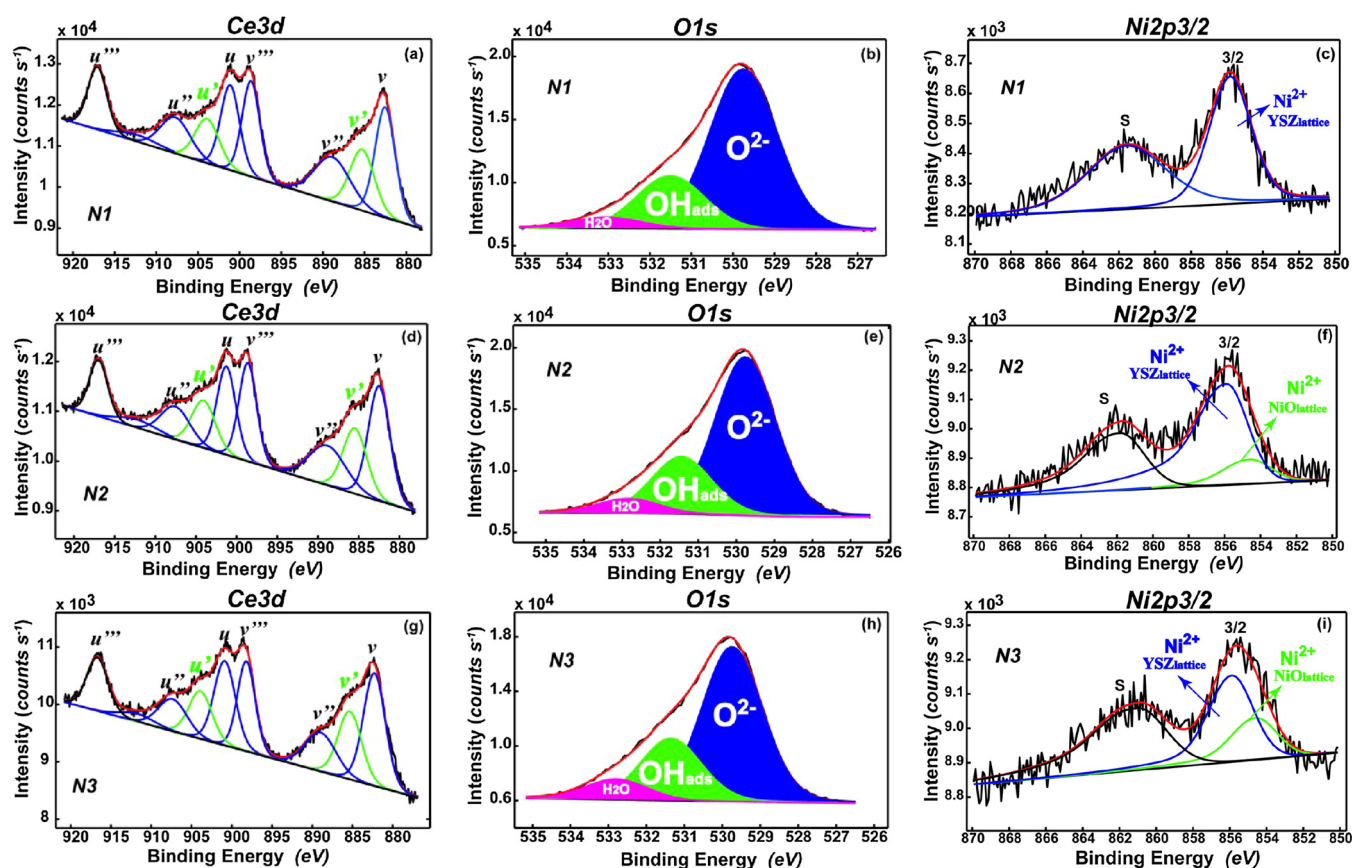


Fig. 8. Ce 3d, O1s and Ni2p3/2 deconvoluted photoelectron spectra for N1, N2, N3 "as prepared" samples. The associated numerical data (binding energies, BEs, and the relative concentrations) are shown in Tables 2a and 2b.

aims were to ascertain their surface chemistry on our N1, N2, N3 "as prepared" samples after calcination (Fig. 8a–i) and after CPOM tests (see Supplementary materials Fig. SI 3), to monitor the degree of surface contamination with carbon, to perform data quantification and to compare the XPS data with the complementary measurements in order to establish links with the catalytic measurements and the associated mechanism.

For XPS data processing and interpretation we use the values of the Binding Energies (BEs) for the photoelectron lines, the presence of the secondary features (e.g. the satellites associated to the main peaks) the peculiarities in the shape of the spectra and standard samples where necessary. It is appropriate to notice that our experimental errors for the Binding Energies (BEs) assignments are within  $\pm 0.2$  eV while for quantitative analysis (relative concentrations) in the range of  $\pm 5\%$ . For lower element relative concentrations ( $< 5$  atom%) the errors expected in quantification increase to  $\pm 10\%$ .

#### 3.4.1. Nickel (Ni2p3/2) chemistry

A likely disagreement appears between XPS analysis (extremely surface sensitive, mainly for Ni element) and the nominal stoichiometry for, especially, N3 sample as well as compared with the EDS results. Just an inspection at a glance (Fig. 8c, f, i) show noisy spectra suggesting lower experimental Ni percentages as compared to the nominal ones, mainly for N3 sample. We estimated the detected "volume" (depth) of Ni in our sample matrix by using the Tougaard's numerical cod [43]. Thus, if the inelastic mean free path (IMFP) of Ni2p photoelectrons in our sample is  $\lambda \sim 1.2$  nm, then the detected volume is  $\sim 3 \lambda = 3.6$  nm.

This means that the XPS probes an outermost surface layer thinner than the size of the crystallites (in the range of (6–10) nm as determined by SEM-TEM analysis and XRD, as well). Therefore, during the

calcination and testing processes Ni could migrate from the surface to the subsurface region and, consequently, the outermost surface layer occurs as depleted in Ni.

Moreover, particularly for N3 sample (the highest Ni relative concentration) the STEM image mapping (Fig. 5) reveals a tendency to form agglomerated grains leading to the shadowing effect in the process of photoelectron emission. This particular, inhomogeneous morphology has the potential to induce an attenuation of the photoemission intensities, that might affect the accuracy of the element composition within a narrow surface layer ( $< 4$  nm) (Fig. 5). As the X-ray beam diameter ( $\sim 100$   $\mu$ m) incident on the surface sample is a lot beyond the SEM/TEM scale, there is enough evidence in the aforementioned arguments that support our experimental results regarding the severe decrease of the Ni content mainly for the sample N3.

The key role of Ni might be the promoting of ceria to the surface showing a sudden increase for the sample N3 as well as of the  $\text{Ce}^{3+}$  percentage (see Table 2a). Despite the large amount of noise in the Ni2p3/2 spectra we performed the spectra deconvolution in order to evidence the species present in modified YSZ. Thus, the chemical species of the nickel confined within a very thin (3–4 nm) surface layer exhibit the presence of  $\text{Ni}^{2+}$  incorporated in the stabilized YSZ lattice for N1 at  $\sim 855.8$  eV. For N2 and N3 samples a mixture of nickel species attributed to  $\text{Ni}^{2+}$  incorporated in the YSZ lattice ( $\sim 855.8$  eV) and  $\text{Ni}^{2+}$  bound in the NiO formed as secondary phase ( $\sim 854.6$  eV) (Fig. 8c, f, i and Tables 2a and 2b) in accordance with XRD results and  $\text{H}_2$ -TPR that provide evidence on the formation of the two type of  $\text{Ni}^{2+}$  species found in N2, N3 samples.

#### 3.4.2. Cerium (Ce3d) chemistry

Ceria exhibits a characteristic 3d band-like spectra (Fig. 8a, d, g) providing evidence for the mixture of 3+/4+ oxidation states. For



**Table 2a**

XPS data: Ni and Ce chemical states relative concentrations (%): Ni-YSZ lattice, NiO, Ni<sup>o</sup>.  $Ce^{3+}(\%) = Ce^{3+} / (Ce^{3+} + Ce^{4+})$  percentages (%) and cation relative concentrations (atom%).

Sample	Ni chemistry			Ce chemistry		Cation relative concentrations (atom %)			
	Ni-YSZ lattice	NiO	Ni <sup>o</sup>	Ce3+ (%)	Ce4+ (%)	Ni	Ce	Y	Zr
N1	100	–	–	20.9	79.1	6.1	21.1	19.4	53.4
N2	83	17	–	22.7	77.3	5.8	23.5	21.6	49.1
N3	67.2	32.8	–	24.1	75.9	7.7	28.3	24.5	39.5
N1	–	77.1	22.9	22.1	77.9	2.1	23.0	22.1	62.0
CPOM									
N2	–	78.8	17.2	24.4	75.6	3.0	24.6	24.4	57.2
CPOM									
N3	25.5	74.5	–	25.7	74.3	4.1	26.3	25.7	46.0
CPOM									

spectral deconvolution process, interpretation and quantification a well established procedure was employed [36,47,48]. The percentages of ceria on the outermost surface layer follow the order (see Tables 2a and 2b): N3 > N2 > N1 suggesting a segregation process from the bulk to the surface in both stages: fresh and spent catalysts. It is appropriate to emphasize the key role of Ce3+ oxidation state which generates oxygen vacancies in the lattice enabling higher oxygen mobility and greatly increasing the ionic conductivity and the oxygen storage capacity. As such, the overall Ce3+ relative concentrations reveal the same order of the samples. As mentioned above the presence of Ce3+ is a result of oxygen vacancies and this effect is enhanced for N3 sample because a larger fraction of the atoms is confined on the surface due to a sudden increase in Ce relative concentrations in N3 samples in both stages (see Tables 2a and 2b). It is worth to mention that the increasing of the oxygen mobility favors the carbon removal [49] supporting our findings in the carbon section (3.4.4).

### 3.4.3. Oxygen (O1s) chemistry

The O1s deconvoluted spectra (Fig. 8b, e, h) display the presence of three main components: oxygen bonded in the lattice (O<sup>2−</sup>), hydroxyl groups and water adsorbed on the surface. These spectra clearly reveal the presence of a hydrous outermost surface layer through the adsorbed hydroxyl groups and water molecules which ensure an enhanced oxygen mobility on the surface layer leading to a higher catalytic activity and minimizing the rate of carbon deposition. The extent of the hydroxylated surfaces linked to (OH+H<sub>2</sub>O) adsorbed relative concentrations follow the order: N3 (34.0%) > N2 (31.8%) > N1 (29.9%) (see Fig. 8b, e, h).

**Table 2b**

XPS data: Binding Energies (BEs - eV).

Sample	Binding energy (eV)						
	Ni-YSZ lattice	NiO	Ni <sup>o</sup>	Ce <sup>3+</sup>	Ce <sup>4+</sup>	Y3d5/2	Zr3d5/2
N1	855.8	–	–	$v' = 885.4$ $u' = 904.0$	882.3 900.9 888.9 907.4 898.2 916.7	157.0	181.9
N2	855.9	854.6	–	$v' = 885.4$ $u' = 904.1$	882.4 901.3 888.8 907.5 898.6 916.9	157.1	181.9
N3	855.8 -	854.6	–	$v' = 885.3$ $u' = 904.0$	882.5 901.2 888.9 907.7 898.6 917.0	157.0	182.0
N1	–	854.7	852.7	$v' = 885.4$ $u' = 904.0$	882.3 901.1 888.9 907.4 898.4 916.8	156.9	181.9
CPOM							
N2	–	854.7	852.6	$v' = 885.4$ $u' = 904.0$	882.3 900.9 888.9 907.3 898.4 916.7	157.0	182.0
CPOM							
N3	855.9	854.7	–	$v' = 885.5$ $u' = 904.0$	882.3 900.9 888.9 907.2 898.3 916.6	157.1	182.0
CPOM							

### 3.4.4. Carbon (C1s)

It is widely accepted that the excessive formation of carbon deposit (“coke”) on the surface of the Ni-based anodes leads to a significant deactivation of the catalysts. Therefore, we explored in detail (elemental relative concentrations and the associated chemical species) the carbon behavior on the surface of our samples in both stages: after calcination and after reaction (Fig. 9a–c). The comparison with a standard NiO-YSZ commercial sample clearly demonstrate the role of the surface chemistry to minimize the carbon deposition. As such, the rate of carbon formation on the surface of our samples was markedly low. Thus, for the calcined samples the percentages of carbon on the surface were in the range of (16–17 atom %) while for the spent samples the carbon relative concentrations slightly increase to 19–20%. Further, the (C–C) species including amorphous carbon, which is the main candidate for the deactivation of the catalytic sites, accounts for ~70% of the total amount of adsorbed/deposited carbon leading to ~12% percentage of carbon on the surface of calcined samples and ~15% for the samples after CPOM test. Clearly, the addition of the carbon during CPOM catalytic test is achieved at a low rate. We emphasize that our synthesis route promotes a direct incorporation of Ni and Ce into YSZ lattice accompanied by a tendency of surface ceria enrichment with increasing Ni content leading to an enhanced carbon tolerance. Moreover, the surface enriching in Ce is accompanied by a higher percentage of Ce<sup>3+</sup> oxidation state (see Tables 2a and 2b) for tested sample, in correlation with TPR analysis, which indicates also that Ce<sup>3+</sup> species were in higher amount after the first cycle of reduction-oxidation. This particular surface chemistry also elevates the rate of carbon oxidation in competition with the rate of carbon

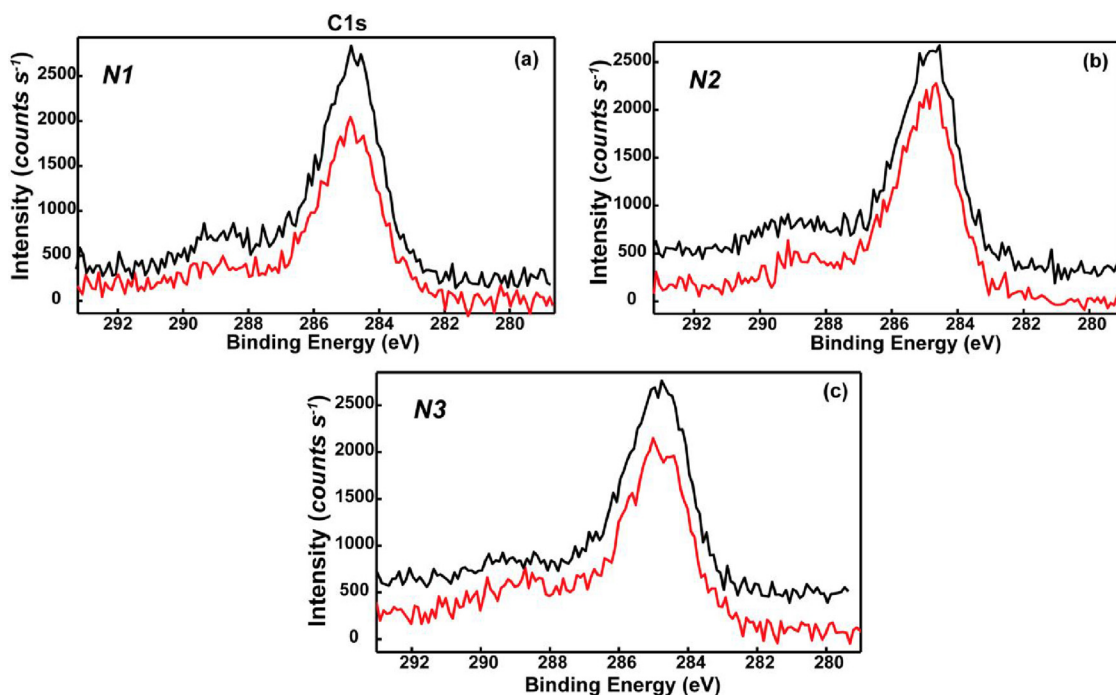


**Fig. 9.** C1s superimposed spectra for “as prepared” (lower) and after (upper) catalytic test for the samples N1 (a), N2 (b), N3 (c). (For interpretation of the references to colour in this figure legend, the reader is referred to the web version of this article).

deposition

### 3.5. Electrochemical assesement

The electrical conductivity of the investigated samples (N1, N2, N3 powders) was evaluated from impedance spectroscopy measurements carried out under reducing mixture 4%, vol. H<sub>2</sub> in Ar, in the temperature range 300–800 °C. The Nyquist plots of EIS spectra for the investigated samples at different temperatures are shown in Fig. 10. The axes were normalized with S/l ratio to allow a proper comparison. In the investigated temperature range, one arc was evidenced in the Nyquist plot of EIS spectra. The capacitance was evaluated to  $\sim 200$  pF cm<sup>-2</sup>, lower than the one of grain boundary processes (in the range of nF cm<sup>-2</sup>). The intercept of this arc with the real axis at low frequency gave the total resistance of the electrolyte, the contributions of bulk and grain boundaries being overlapped due to their similar relaxation times of charge carriers.

The electrolyte conductivity ( $\sigma$ ) was calculated from the electrolyte resistance using the following equation:

$$\sigma = \frac{1}{R} \times \frac{l}{S}$$

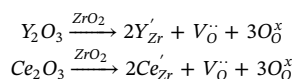
where  $l$  and  $S$  are the sample thickness and electrode area, respectively.

The conduction process is thermally activated and the activation energy can be evaluated using the equation:

$$\sigma = \frac{\sigma_0}{T} \exp\left(-\frac{E_a}{kT}\right),$$

where  $\sigma$  is the ionic conductivity,  $\sigma_0$  – pre-exponential factor,  $T$  – absolute temperature,  $E_a$  – activation energy, and  $k$  – Boltzmann constant.

It is well-known that doping zirconia with a proper amount of yttria led to the stabilization of cubic phase at low temperatures. Moreover, this process together with Ce<sup>3+</sup> substitution, leads to oxygen vacancies generation according to the following equations written in Kröger-Vink notation:



Moreover, reduction of NiO to Ni occurs under reducing atmosphere, as TPR measurements evidenced.

There are several factors strongly affecting the electrical conductivity of Ni-based cermet anode materials, such as particle size, distribution of Ni, ceramic components, the Ni/ceramic ratio, sintering conditions [50]. Arrhenius plots of the total conductivity under reducing atmosphere for the investigated samples are shown in Fig. 11. There are two factors contributing to the increase in the electrical conductivity in the order N1 < N2 < N3: (i) the increase in trivalent ions concentration and (ii) the increase in Ni content, respectively.

Only one activation energy was obtained for each sample in the investigated temperature range. The activation energies of conduction were evaluated to 0.72 eV, 0.70 eV and 0.66 eV for N1, N2 and N3, respectively. These values are characteristic to mixed ionic-electronic conduction. The ionic conductivity of YSZ shows an activation energy of 1.0–1.2 eV [51] while Ni/YSZ composite exhibited different activation energies depending on Ni content and temperature range [52].

### 3.6. Catalytic activity measurements

The catalytic oxidation of methane over the mesoporous powder was carried out at different temperatures varying between 300 °C and 800 °C, using CH<sub>4</sub>/O<sub>2</sub> feed ratio of 2 at a GHSV of 22,500 h<sup>-1</sup>. In order to avoid hot-spots in the catalyst bed and for better temperature control, N<sub>2</sub> was used to dilute the reactant gas mixture and quartz powder was mixed with the catalyst. Blank tests performed in the presence of quartz powder and using the same reaction parameters as during the catalyst screening showed no detectable occurrence of homogeneous reactions. Fig. 12 presents the effect of temperature on the catalytic activity. The methane conversion values were taken after 30 min of reaction at each temperature. Products of methane oxidative coupling (C<sub>2</sub> and higher hydrocarbons) have not been observed on the entire temperature range.

Preliminary experiments using a pre-treatment were done. In Fig. S1

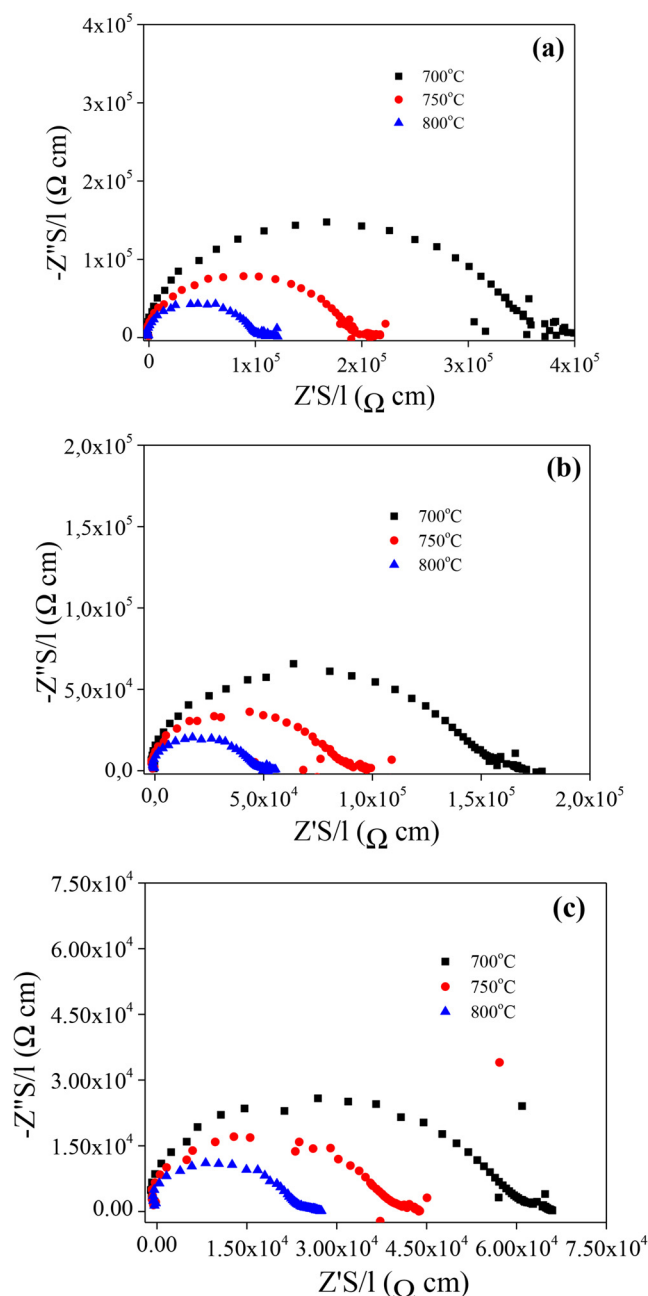


Fig. 10. Nyquist plots of EIS spectra for N1 (a), N2 (b), N3 (c) powders.

4 are presented the results obtained for N1 sample reduced in  $H_2$  at 600 °C and unreduced one prior to catalytic tests. Both the unreduced and pre-reduced catalyst showed similar activity and selectivity for CPOM at higher temperatures, and only the light-off temperature is different. Similar results were obtained by other groups [53,54] and they suggested that in fact the active sites are formed by the catalyst reduction with  $CH_4$  and the formation of surface carbon species, process that is less important on the catalysts already reduced by  $H_2$ . There are studies that suggest that adsorbed carbon may be the intermediate for the formation of CO [14,55]. In the light of these experiments the catalytic performances presented further are obtained on the samples that were not reduced prior reaction.

The conversion profile recorded on the studied samples for the catalytic partial oxidation of methane (see Fig. 12) showed that these materials are active above 400 °C (with one exception for N3 sample at above 300 °C) with methane completely converted at 850 °C and with a selectivity of almost 100% in CO. At low temperature, the complete

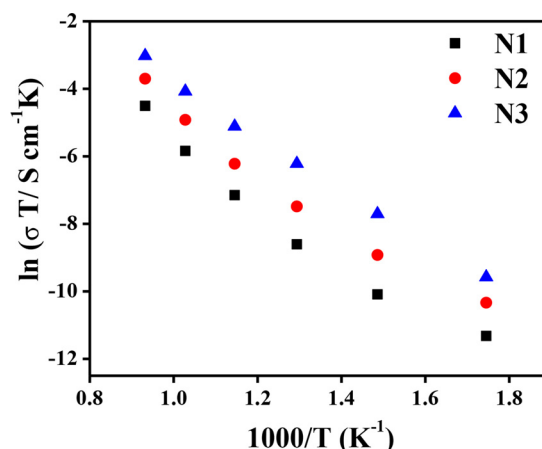


Fig. 11. Arrhenius plots of total electric conductivity for the investigated samples.

oxidation of methane to  $CO_2$  and  $H_2O$  occurs on the ceria surface [56], while with the increasing of the temperature, CO and  $H_2$  are formed on reduced ceria [55]. Nevertheless, it is well known that nickel is the active component for CPOM and therefore the amount of Ni plays an important role and some peculiarities are observed as a function of the Ni loading, as following: i) the  $O_2$  consumption starts for N3 sample at lower temperature (above 200 °C) and also is totally converted at lower temperature (600 °C) with respect to the N1 system (above 300 °C and 700 °C respectively); ii) the methane is 100% converted at 800 °C for the N3 sample, while N1 and N2 provide a methane conversion of 85.8 and 94.6%, respectively at the same temperature; iii) the CPOM light-off temperature, where CO and  $H_2$  start to be formed depends on the Ni loading (i.e. above 500, 400 and 300 °C for N1, N2 and N3 respectively), while only complete oxidation products,  $CO_2$  and  $H_2O$ , were formed at lower temperatures. Also, the reduction onset temperature (second TPR cycle) correlates well with the light-off temperature for CPOM.

To summarize, the sample containing higher amount of Ni (N3 with 15%) is the most active one, the catalytic performance being related to the surface area, the amount of surface Ni available, the amount of  $Ce^{3+}$ , together with the different oxidative state of Ni. Indeed, if we correlate the catalytic activity with the characterization data it can be observed that N1, the less active material, did not present NiO on the surface (as observed from XPS and TPR data) and the only detected phase in XRD is a main phase with fluorite-type symmetry, attributed to NiCeYZ phase, while for the N3 material, with the highest Ni loading (15%), the TPR analysis revealed two types of reducible nickel species: segregate NiO at low temperature and Ni inserted in the YSZ lattice at high temperature in agreement with the surface analysis performed by XPS technique. Along with this, the TPR indicates that the samples with higher amount of Ni (N2 and N3) possess also a higher oxygen mobility and these samples contain higher amount of  $Ce^{3+}$  as revealed also by XPS analysis. Another factor that may promote the catalytic activity of this type of materials is the strength of the interaction between Ni and support. According to Takeguchi et al. the interaction between nickel species and oxygen vacancies may create active Ni- $Ce^{3+}$  centers by a synergetic effect [44]. This interaction may be responsible for the increase of the catalytic activity, since the vacancies activate the oxygen species. Also, for N3 sample the  $O_2$  consumption starts at low temperature (see Fig. 12), indicating that the amount of nickel could be responsible for the oxygen activation. Higher Ni content implies more intimate contact between Ni and support, improving the probable oxygen transfer from lattice to Ni [57,58]. Also, even that the cerium loading is the same for all samples, the XPS analysis, shows that the  $Ce^{3+}$  relative concentration is increasing with Ni loading, and the catalytic activity increases too (Fig. SI 5).



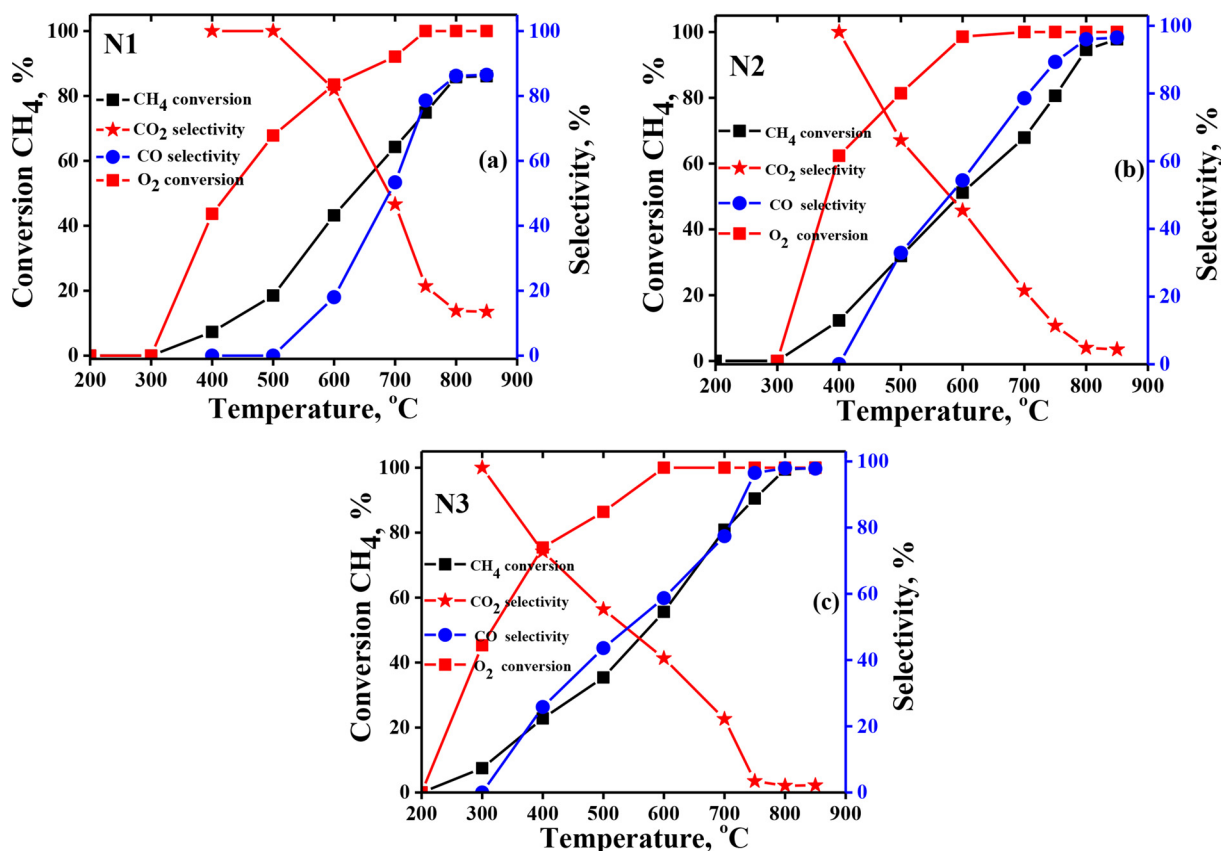


Fig. 12. Methane conversion for CPOM for the N1 (a) N2 (b) and N3 (c) “as prepared” samples at different reaction temperatures ( $\text{CH}_4/\text{O}_2$  feed ratio of 2 at a GHSV of  $22,500 \text{ h}^{-1}$ ).

Additionally, a sample with higher Ni loading (30 mol%) was tested and the results are presented in the supplementary material, Fig. SI 6. The conversion decreases drastically after only 5 h time on stream from 52% to 30% and remains stable for 72 h. The selectivity is also altered during the time on stream and CO selectivity increases gradually. Such unusual behaviour could be explained probably by the coexistence of endothermic and exothermic processes (eq. 1 and eq. 2) whose extent depends on heat transport [59]. However, the XPS analysis of the tested N4 sample revealed very low amount of coke formation, indicating a very high tolerance to carbon formation during CPOM. A possible explanation for this comportment could be the high hydroxylation degree of the surface, well known to prevent coke formation. This is a very

interesting result that will be elaborated in a further study.

The catalytic tests over time were performed by directly ramping to  $800^\circ\text{C}$  without passing through intermediate temperatures, using a stoichiometric  $\text{CH}_4/\text{O}_2$  feed ratio of 2 at a GHSV of  $22,500 \text{ h}^{-1}$ . As can be observed in Fig. 13, the stability of the studied sample is also depending on the Ni loading.

The most stable catalyst is the one containing the highest amount of Ni, the N3 sample. Several reasons were identified to be responsible for this behavior: i) the enhanced reducibility of the  $\text{Ce}^{4+}$  as observed from the shift of the reduction temperature to lower values as compared with the standard. ii) the amount of  $\text{Ni}^{2+}$  species is higher than other samples (from XPS and XRD). Also, the highest stability of the N3 sample could be attributed to the enhanced transfer of oxygen from ceria to the nickel interface, oxidizing the carbon species deposited on nickel. Therefore, the higher degree of reducibility of cerium, with the generation of oxygen vacancies, can play a key role in this reaction. The N3 sample is stable even after 72 h, as presented in Fig. SI 6.

Nevertheless, our results are in agreement with the one of Takeguchi et al. which demonstrated that the Ni particles having a weak interaction with the support had a metallic feature and produced large amounts of coke, whereas the Ni particles having a strong interaction with the support had a cationic nature and produced a small amount of coke [40]. Indeed, the most stable sample is N3 which seems to present Ni in a strong interaction with the lattice. Additionally, from the XPS analysis of the spent catalysts it can be observed that no  $\text{Ni}^0$  was identified on the surface on N3 sample, while for N1 and N2 samples small amount of  $\text{Ni}^0$  were evidenced (see Table 2a).

Fig. 14 depicts the evolution in time of CO and  $\text{CO}_2$  selectivities for the studied samples in CPOM at  $800^\circ\text{C}$ . Besides CO formation due to partial selective oxidation of  $\text{CH}_4$ , is observed  $\text{CO}_2$  formation due to the complete oxidation of methane for all samples, but the selectivity profiles are different, depending on the catalyst composition. Thus, the

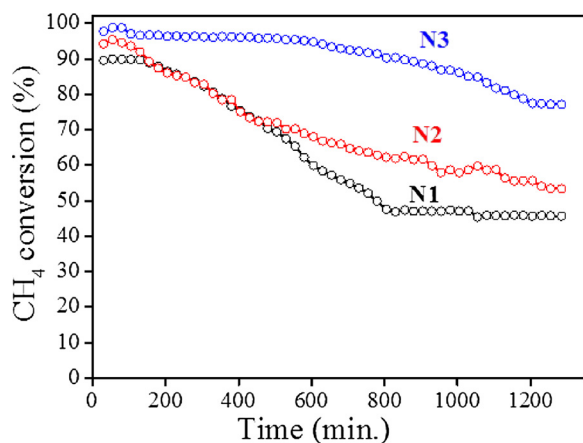


Fig. 13. Evolution in time of methane conversion on the “as prepared” samples ( $800^\circ\text{C}$ ,  $\text{CH}_4/\text{O}_2$  feed ratio of 2 at a GHSV of  $22,500 \text{ h}^{-1}$ ).

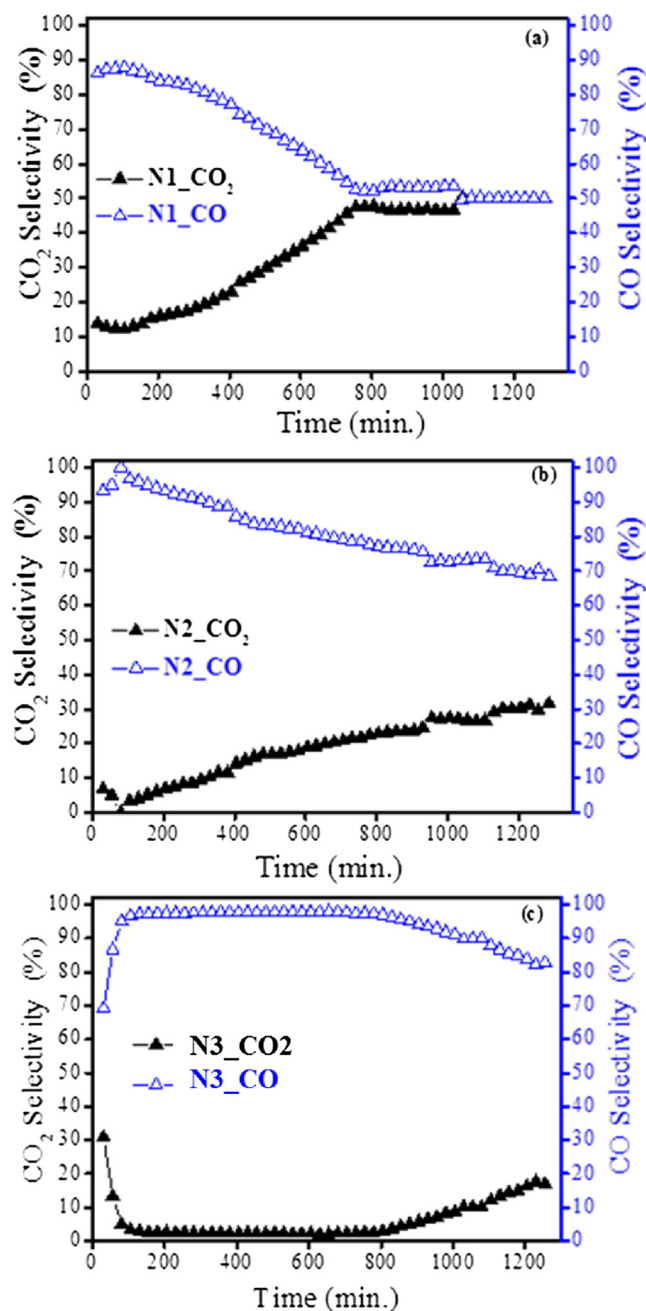


Fig. 14. CO and CO<sub>2</sub> selectivities on N1(a) N2 (b) and N3 (c) “as prepared” samples (800 °C, CH<sub>4</sub>/O<sub>2</sub> = 2 at a GHSV of 22,500 h<sup>-1</sup>).

most selective catalyst is the one with the highest content in Ni, the N3 sample, which also present an induction period of about 150 min (Fig. 12c) to reach the 100% selectivity to CO, which is kept for about 13 h. The induction period can be justified by the time needed for the reduction of Ce<sup>4+</sup> to Ce<sup>3+</sup> in the presence of CH<sub>4</sub> with the formation of oxygen vacancies that could represent active centers for CPOM. This assumption is supported by the XPS analysis, which shows and increases of the Ce<sup>3+</sup> relative concentration for spent catalysts (Fig SI 3). This was also already reported in our previous work on ceria based catalysts for which such a behavior with time on stream for long-term reaction was evidenced [60]. Changes in the redox properties have been proposed as the major cause, and demonstrated by CH<sub>4</sub>- temperature programmed reduction.

#### 4. Conclusions

The report describes an advantageous and advanced hydrothermal synthesis route in the preparation of the bimodal mesoporous NiO/CeO<sub>2-δ</sub>-YSZ (5, 10 and 15 mol% Ni; 20% mol.% Ce) anodes with enhanced carbon tolerance in the catalytic partial oxidation of methane. The materials were successfully direct synthesized by using CTAB and TPA as templates by a hydrothermal route. In particular, we design, by our innovative approach, anodes with high concentration of Ce<sup>3+</sup> ions (21–28%) generated by increase of Ni amount, in the as prepared samples. From XRD analysis and HRTEM images was found that for the lowest Ni amount a solid solution with cubic fluorite type structure is formed proving that Ni is well incorporated in the lattice. Furthermore, the increase of the Ni content leads to the separation of NiO as secondary phase and a decreasing of the crystallite sizes from 7.4 nm to 6.0 nm, additionally confirmed by SAED and EDS mapping. Moreover, the segregation of NiO as secondary phase influence the porous structure and determine mesoporous NiO/CeO<sub>2-δ</sub>-YSZ with bimodal pore size distribution (~6 and ~11 nm).

Electrochemical impedance spectroscopy measurements highlighted a mixed ionic-electronic conduction. The increase of the Ce<sup>3+</sup> percentage as well as the NiO formation facilitate the improvement of the electrical conductivity. A similar behavior was observed for the catalytic activity. The aforementioned materials are highly active and selective catalysts for partial oxidation of methane to syngas at temperatures higher than 550 °C. This behaviour is explained by reducibility of these powders as assessed by TPR, induced by the presence of Ni and Ce which improve the oxygen mobility in the YSZ lattice. Moreover, the types of Ni species and the ratio between these species and Ce<sup>3+</sup> ones, as highlighted by XPS analysis, play also a key role on the CH<sub>4</sub> catalytic conversion and CO selectivity.

In conclusion, NiO/CeO<sub>2-δ</sub>-YSZ (15%mol.%) with larger surface area, higher reducibility degree, the optimal ratio between the two types of Ni<sup>2+</sup> species and higher Ce<sup>3+</sup> percentage, showed excellent resistance to carbon deposition and a high stability over long time operating period. This finding is supported by comprehensive XPS analysis that have monitored the carbon deposition in both stages (before and after CPOM tests) and the peculiarities of the surface chemistry, as well. Hence, a new avenue may be opened for the use of these bimodal mesoporous anodes in the IT-SOFCs. Depending on the used fuel and the working conditions, the electrochemical and catalytic properties could be further tailored.

Our findings open a new perspective on the assessment of the anodes with higher Ni content (20–30 mol%). Preliminary results obtained for an increased Ni content (30 mol.%) highlighted the formation of the mesoporous structure with a lower specific surface, probably due to the increased NiO percentage as secondary phase. A very good dispersion of Ni as well as a strong hydroxylated surface lead to a remarkable carbon tolerance after long time operation (CPOM for 72 h). However, much work should be devoted to optimizing the synthesis protocol in view of the properly Ni incorporation as well as to expand the range of catalytic tests (e.g. dry reforming of methane).

#### Acknowledgements

This work was funded by the Romanian National Authority for Scientific Research through the Partnerships in priority S&T domains Program (PNII), MEN-UEFISCDI, Project number 26/2012; Romanian National Authority for Scientific Research and Innovation, CNCS UEFISCDI projects PN-III-P4-ID-PCE-2016-0692 and PN-III-P4-ID-PCE-2016-0529, within PNCDI III and CNCS/CCCDI-UEFISCDI project number PN-III-P2-2.1-PED-2016-1429, within PNCDI III.

MF, FN and CG acknowledge Romanian Ministry of Research and Innovation through the Core Program PN18-110101.

## Appendix A. Supplementary data

Supplementary material related to this article can be found, in the online version, at doi:<https://doi.org/10.1016/j.apcatb.2018.09.065>.

## References

- [1] H. Kan, H. Lee, Sn-doped Ni/YSZ anode catalysts with enhanced carbon deposition resistance for an intermediate temperature SOFC, *Appl. Catal. B Environ.* 97 (2010) 108–114.
- [2] A.L. Vincent, J.-L. Luo, K.T. Chuang, A.R. Sanger, Promotion of activation of CH<sub>4</sub> by H<sub>2</sub>S in oxidation of sour gas over sulfur tolerant SOFC anode catalysts, *Appl. Catal. B Environ.* 106 (2011) 114–122.
- [3] E.V. Kondratenko, M. Baerns, Catalysis of Oxidative Methane Conversions, *Nanostructured Catalysts*, (2011), pp. 35–55.
- [4] J.R. Webb, T. Bolaño, T.B. Gunnoe, Catalytic oxy-functionalization of methane and other hydrocarbons: fundamental advancements and new strategies, *ChemSusChem* 4 (2011) 37–49.
- [5] A.I. Olivos-Suarez, Ag. Szécsényi, E.J. Hensen, J. Ruiz-Martinez, E.A. Pidko, J. Gascon, Strategies for the direct catalytic valorization of methane using heterogeneous catalysis: challenges and opportunities, *ACS Catal.* 6 (2016) 2965–2981.
- [6] J.R. Rostrup-Nielsen, J. Sehested, J.K. Nørskov, Hydrogen and Synthesis Gas by Steam and CO<sub>2</sub> Reforming, (2002).
- [7] R.M. Navarro, M. Pena, J. Fierro, Hydrogen production reactions from carbon feedstocks: fossil fuels and biomass, *Chem. Rev.* 107 (2007) 3952–3991.
- [8] M. Prett, C. Eichner, M. Perrin, The catalytic oxidation of methane to carbon monoxide and hydrogen, *Trans. Faraday Soc.* 42 (1946) 335b–339.
- [9] W. Vermeiren, E. Blomsma, P. Jacobs, Catalytic and thermodynamic approach of the oxyreforming reaction of methane, *Catal. Today* 13 (1992) 427–436.
- [10] T. Hayakawa, A.G. Andersen, M. Shimizu, K. Suzuki, K. Takehira, Partial oxidation of methane to synthesis gas over some titanates based perovskite oxides, *Catal. Lett.* 22 (1993) 307–317.
- [11] A. Ashcroft, A. Cheetham, Ja. Foord, M. Green, C. Grey, A. Murrell, Selective oxidation of methane to synthesis gas using transition metal catalysts, *Nature* 344 (1990) 319.
- [12] P.D. Vernon, M.L. Green, A.K. Cheetham, A.T. Ashcroft, Partial oxidation of methane to synthesis gas, *Catal. Lett.* 6 (1990) 181–186.
- [13] R.H. Jones, A.T. Ashcroft, D. Waller, A.K. Cheetham, J.M. Thomas, Catalytic conversion of methane to synthesis gas over europium iridate, *Eu 2 Ir 2 O 7: an in situ study by x-ray diffraction and mass spectrometry*, *Catal. Lett.* 8 (1991) 169–174.
- [14] D. Hickman, L. Schmidt, Production of syngas by direct catalytic oxidation of methane, *Science* 259 (1993) 343–346.
- [15] P. Tornaiainen, X. Chu, L. Schmidt, Comparison of monolith-supported metals for the direct oxidation of methane to syngas, *J. Catal.* 146 (1994) 1–10.
- [16] J. Milewski, SOFC hybrid system optimization using an advanced model of fuel cell, *Sustainable Research and Innovation Proceedings vol. 3*, (2011).
- [17] D.R. Rolison, Catalytic nanoarchitectures—the importance of nothing and the unimportance of periodicity, *Science* 299 (2003) 1698–1701.
- [18] M. Mori, Y. Hiei, H. Itoh, G.A. Tompsett, N.M. Sammes, Evaluation of Ni and Ti-doped Y<sub>2</sub>O<sub>3</sub> stabilized ZrO<sub>2</sub> cermet as an anode in high-temperature solid oxide fuel cells, *Solid State Ion.* 160 (2003) 1–14.
- [19] X. Zhou, J. Zhen, L. Liu, X. Li, N. Zhang, K. Sun, Enhanced sulfur and carbon coking tolerance of novel co-doped ceria based anode for solid oxide fuel cells, *J. Power Sources* 201 (2012) 128–135.
- [20] M. Mogensen, D. Lybye, N. Bonanos, P. Hendriksen, F. Poulsen, Factors controlling the oxide ion conductivity of fluorite and perovskite structured oxides, *Solid State Ion.* 174 (2004) 279–286.
- [21] C. Solis, M. Balaguer, F. Bozza, N. Bonanos, J. Serra, Catalytic surface promotion of highly active La<sub>0.85</sub>Sr<sub>0.15</sub>Co<sub>0.8</sub>Ni<sub>0.2</sub>O<sub>3-δ</sub> anodes for La<sub>0.5</sub>WO<sub>3.5</sub> 4–δ based proton conducting fuel cells, *Appl. Catal. B Environ.* 147 (2014) 203–207.
- [22] S. Sengodan, S. Choi, A. Jun, T.H. Shin, Y.-W. Ju, H.Y. Jeong, J. Shin, J.T. Irvine, G. Kim, Layered oxygen-deficient double perovskite as an efficient and stable anode for direct hydrocarbon solid oxide fuel cells, *Nat. Mater.* 14 (2015) 205.
- [23] C. Périllat-Merceroz, G. Gauthier, P. Roussel, M. Huvé, P. Gélén, R.-N. Vannier, Synthesis and study of a Ce-doped La/Sr titanate for solid oxide fuel cell anode operating directly on methane, *Chem. Mater.* 23 (2011) 1539–1550.
- [24] N. Cioatera, E.A. Voinea, E. Panaintescu, A. Rolle, S. Somacescu, C.I. Spinu, R.N. Vannier, Changes in structure and electrical conductivity of rare-earth titanate pyrochlores under highly reducing atmosphere, *Ceram. Int.* 42 (1) (2016) 1492–1500.
- [25] Q. Ma, B. Iwanschitz, E. Dashjav, S. Baumann, D. Sebold, I.A. Raj, A. Mai, F. Tietz, Microstructural variations and their influence on the performance of solid oxide fuel cells based on yttrium-substituted strontium titanate ceramic anodes, *J. Power Sources* 279 (2015) 678–685.
- [26] D. Flot, J. Irvine, Synthesis, electrical properties and thermal analysis of transition metal-doped Mg<sub>2</sub>TiO<sub>4</sub> spinels, *Solid State Ion.* 135 (2000) 513–518.
- [27] P. Holtappels, F. Poulsen, M. Mogensen, Electrical conductivities and chemical stabilities of mixed conducting pyrochlores for SOFC applications, *Solid State Ion.* 135 (2000) 675–679.
- [28] E. Tsipis, V. Kharton, J. Frade, Mixed conducting components of solid oxide fuel cell anodes, *J. Eur. Ceram. Soc.* 25 (2005) 2623–2626.
- [29] D.H. Prasad, H.-I. Ji, H.-R. Kim, J.-W. Son, B.-K. Kim, H.-W. Lee, J.-H. Lee, Effect of nickel nano-particle sintering on methane reforming activity of Ni-CGO cermet anodes for internal steam reforming SOFCs, *Appl. Catal. B Environ.* 101 (2011) 531–539.
- [30] A. Da Silva, N. Bion, F. Epron, S. Baraka, F. Fonseca, R. Rabelo-Neto, L. Mattos, F. Noronha, Effect of the type of ceria dopant on the performance of Ni/CeO<sub>2</sub> SOFC anode for ethanol internal reforming, *Appl. Catal. B Environ.* 206 (2017) 626–641.
- [31] V.B. Vert, F.V. Melo, L. Navarrete, J.M. Serra, Redox stability and electrochemical study of nickel doped chromites as anodes for H<sub>2</sub>/CH<sub>4</sub>-fueled solid oxide fuel cells, *Appl. Catal. B Environ.* 115 (2012) 346–356.
- [32] Z. Zhang, X.E. Verykios, Carbon dioxide reforming of methane to synthesis gas over Ni/La<sub>2</sub>O<sub>3</sub> catalysts, *Appl. Catal. A Gen.* 138 (1996) 109–133.
- [33] X.E. Verykios, Catalytic dry reforming of natural gas for the production of chemicals and hydrogen, *Int. J. Hydrogen Energy* 28 (2003) 1045–1063.
- [34] A.N. Fatsikostas, D.I. Kondarides, X.E. Verykios, Steam reforming of biomass-derived ethanol for the production of hydrogen for fuel cell applications, *Chem. Commun.* (2001) 851–852.
- [35] S. Somacescu, M. Florea, P. Osiceanu, J.M. Calderon-Moreno, C. Ghica, J.M. Serra, Ni-doped (CeO<sub>2</sub> 2-δ)-YSZ mesoarchitectured with nanocrystalline framework: the effect of thermal treatment on structure, surface chemistry and catalytic properties in the partial oxidation of methane (CPOM), *J. Nanopart. Res.* 17 (2015) 426.
- [36] S. Somacescu, P. Osiceanu, J.M.C. Moreno, L. Navarrete, J.M. Serra, Mesoporous nanocomposite sensors based on Sn<sub>1-x</sub>Ce<sub>x</sub>O<sub>2-δ</sub> metastable solid solution with high percentage of Ce<sup>3+</sup> valence state for selective detection of H<sub>2</sub> and CO, *Microporous Mesoporous Mater.* 179 (2013) 78–88.
- [37] C. Rotaru, G. Postole, M. Florea, F. Matei-Rutkovska, V. Părvulescu, P. Gelin, Dry reforming of methane on ceria prepared by modified precipitation route, *Appl. Catal. A Gen.* 494 (2015) 29–40.
- [38] R.D. Shannon, Revised effective ionic radii and systematic studies of interatomic distances in halides and chalcogenides, *Acta Crystallogr. Sect. A* 32 (1976) 751–767.
- [39] V. Perrichon, A. Laachir, G. Bergeret, R. Fréty, L. Tournayan, O. Touret, Reduction of cerias with different textures by hydrogen and their reoxidation by oxygen, *J. Chem. Soc. Faraday Trans.* 90 (1994) 773–781.
- [40] A. Trovarelli, Catalytic properties of ceria and CeO<sub>2</sub>-containing materials, *Catal. Rev.* 38 (1996) 439–520.
- [41] S. Wang, G.M. Lu, Role of CeO<sub>2</sub> in Ni/CeO<sub>2</sub>-Al<sub>2</sub>O<sub>3</sub> catalysts for carbon dioxide reforming of methane, *Appl. Catal. B Environ.* 19 (1998) 267–277.
- [42] T.A. Maia, E.M. Assaf, Catalytic features of Ni supported on CeO<sub>2</sub>-ZrO<sub>2</sub> 2 solid solution in the steam reforming of glycerol for syngas production, *RSC Adv.* 4 (2014) 31142–31154.
- [43] P. Sermon, G. Bond, Hydrogen spillover, *Catal. Rev.* 8 (1974) 211–239.
- [44] T. Takeguchi, S.-n. Furukawa, M. Inoue, Hydrogen spillover from NiO to the large surface area CeO<sub>2</sub>-ZrO<sub>2</sub> solid solutions and activity of the NiO/CeO<sub>2</sub>-ZrO<sub>2</sub> catalysts for partial oxidation of methane, *J. Catal.* 202 (2001) 14–24.
- [45] F. Fajardie, J.-M. Manoli, G. Djega-Mariadassou, G. Blanchard, Ceria lattice oxygen substitution by Cl—during the reduction of Rh (Cl)/CeO<sub>2</sub> catalysts. Formation and stability of CeOCl, *J. Chem. Soc. Faraday Trans.* 94 (1998) 3727–3735.
- [46] P. Zimmer, A. Tschöpe, R. Birringer, Temperature-programmed reaction spectroscopy of ceria- and Cu/ceria-supported oxide catalyst, *J. Catal.* 205 (2002) 339–345.
- [47] S. Somacescu, V. Părvulescu, P. Osiceanu, J.M. Calderon-Moreno, B.-L. Su, Structure and surface chemistry in crystalline mesoporous (CeO<sub>2</sub> – δ)-YSZ, *J. Colloid Interface Sci.* 363 (2011) 165–174.
- [48] H. Borchert, Y.V. Frolova, V.V. Kaichev, I.P. Prosvirnin, G.M. Alikina, A.I. Lukashevich, V.I. Zaikovskii, E.M. Moroz, S.N. Trukhan, V.P. Ivanov, Electronic and chemical properties of nanostructured cerium dioxide doped with praseodymium, *J. Phys. Chem. B* 109 (2005) 5728–5738.
- [49] G. Pantaleo, V. La Parola, F. Deganello, R. Singha, R. Bal, A. Venezia, Ni/CeO<sub>2</sub> catalysts for methane partial oxidation: synthesis driven structural and catalytic effects, *Appl. Catal. B Environ.* 189 (2016) 233–241.
- [50] X. Weng, D. Brett, V. Yufit, P. Shearing, N. Brandon, M. Reece, H. Yan, C. Tighe, J.A. Darr, Highly conductive low nickel content nano-composite dense cermets from nano-powders made via a continuous hydrothermal synthesis route, *Solid State Ion.* 181 (2010) 827–834.
- [51] A. Chronos, B. Yildiz, A. Tarancón, D. Parfitt, J.A. Kilner, Oxygen diffusion in solid oxide fuel cell cathode and electrolyte materials: mechanistic insights from atomistic simulations, *Energy Environ. Sci.* 4 (2011) 2774–2789.
- [52] Y.M. Park, G.M. Choi, Mixed ionic and electronic conduction in YSZ-NiO composite, *J. Electrochem. Soc.* 146 (1999) 883–889.
- [53] V.R. Choudhary, A.M. Rajput, V.H. Rane, Low-temperature catalytic selective partial oxidation of methane to carbon monoxide and hydrogen over nickel/yttrium sesquioxide, *J. Phys. Chem.* 96 (1992) 8686–8688.
- [54] T. Zhu, M. Flytzani-Stephanopoulos, Catalytic partial oxidation of methane to synthesis gas over Ni-CeO<sub>2</sub>, *Appl. Catal. A Gen.* 208 (2001) 403–417.
- [55] K. Otsuka, Y. Wang, E. Sunada, I. Yamanaka, Direct partial oxidation of methane to synthesis gas by cerium oxide, *J. Catal.* 175 (1998) 152–160.
- [56] L. Kundakovic, M. Flytzani-Stephanopoulos, Cu- and Ag-modified cerium oxide catalysts for methane oxidation, *J. Catal.* 179 (1998) 203–221.
- [57] C.D. Dave, K. Pant, Renewable hydrogen generation by steam reforming of glycerol over zirconia promoted ceria supported catalyst, *Renew. Energy* 36 (2011) 3195–3202.
- [58] J. Chen, Q. Wu, J. Zhang, J. Zhang, Effect of preparation methods on structure and performance of Ni/CeO<sub>2</sub> 75ZrO<sub>2</sub> 25O<sub>2</sub> catalysts for CH<sub>4</sub>-CO<sub>2</sub> reforming, *Fuel* 87 (2008) 2901–2907.
- [59] M. Pena, B. Pawelec, P. Terroeros, J. Fierro, J. Lezaun, J. Gomez, J. Jimenez, S. Vic, Partial oxidation of methane to syngas over Ni-loaded ultrastable HY zeolite catalysts, *Studies in Surface Science and Catalysis*, Elsevier, 1997, pp. 441–446.
- [60] M. Florea, G. Postole, F. Matei-Rutkovska, A. Urda, F. Neațu, L. Massin, P. Gelin, Influence of Gd and Pr doping on the properties of ceria: texture, structure, redox behaviour and reactivity in CH<sub>4</sub>/H<sub>2</sub>O reactions in the presence of H<sub>2</sub>S, *Catal. Sci. Technol.* 8 (2018) 1333–1348.